SENSORS
AND
ACTUATORS
A
PHYSICAL

# A micromachined magnetic-field sensor based on an electron tunneling displacement transducer

D. DiLella [a,*], L.J. Whitman [a], R.J. Colton [a], T.W. Kenny [b,1], W.J. Kaiser [b,2], E.C. Vote [b], J.A. Podosek [b], L.M. Miller [b]

[a] *Code 6170, Naval Research Laboratory, Washington, DC 20375-5342, USA*
[b] *Center of Space Microelectronics Technology, Jet Propulsion Laboratory, California Institute of Technology, Pasadena, CA 91109, USA*

## Abstract

We describe a micromachined magnetic-field sensor that is based on an electron tunneling transducer. This tunnel sensor is small, very sensitive, operates at ambient temperature and requires very little power. The measured resolution of the sensor is $0.3$ nT$/\sqrt{\text{Hz}}$ at 1 Hz. The limiting resolution, calculated based on fundamental noise sources, is $0.002$ nT$/\sqrt{\text{Hz}}$ at 1 Hz. The dominant source of the observed noise in the present device is low frequency air pressure fluctuations. © 2000 Published by Elsevier Science B.V.

*Keywords:* Magnetic-field sensor; Tunnel sensor; MEMS

## 1. Introduction

The remarkable displacement sensitivity of the scanning tunneling microscope (STM) has inspired the development of a new class of sensors. These devices, called tunnel sensors, are based on electron tunneling displacement transducers [1]. For these transducers, displacement is measured by the change in tunnel current between two electrodes. Tunnel sensors have several attractive properties. The most important of these is a large sensitivity to very small changes in the separation between a pair of metallic electrodes. The current between the electrodes is governed by quantum mechanical tunneling and depends exponentially on the gap between the electrodes. Typically, the tunnel junction is biased at a few hundred millivolts and the gap is set to maintain a tunneling current of about 1 nA. This corresponds to a tunneling gap of about 1 nm. For gold electrodes in room air, a change in electrode separation of 0.003 nm results in a 1% change in tunneling current. A change of this magnitude is easily

detected using an electronic feedback control circuit built with inexpensive high-input impedance amplifiers. Because the tunneling current is localized to a small area, the tunneling electrodes may be miniaturized considerably [2,3]. With modern silicon micromachining techniques, mechanical structures with micron dimensions are readily achieved. The displacement sensitivity of the tunneling transducer allows a micromechanical structure to offer sensor performance normally obtained only from much larger devices. Consequently, tunneling displacement transducers offer a new opportunity for the miniaturization of a broad class of physical sensors.

Several tunnel sensors have been built or proposed. In 1987, Niksch and Binnig [4] first proposed using a tunneling displacement transducer for measuring gravitational waves collected by whip or horn-shaped transformers. They believed that the tunneling transducer might allow one to build a sensor to reach the fundamental limits determined by thermal and quantum noise. In the following year, in back-to-back publications, two prototypes for electron tunneling sensors were introduced, an accelerometer [5] and magnetic-field sensor [6]. Waltman and Kaiser [5] used tunneling to measure the displacement of a cantilever-supported proof mass under acceleration of the sensor structure. Their prototype accelerometer had a noise-limited resolution of $10^{-6}$ g$/\sqrt{\text{Hz}}$ and a bandwidth of approximately 3 kHz. A micromachined version of the

---

* Corresponding author. Department of Chemistry, Shepherd College, Shepherdstown, WV 25443, USA.
[1] Present address: Department of Mechanical Engineering, Stanford University, Stanford, CA 94305, USA.
[2] Present address: Department of Electrical Engineering, University of California-Los Angeles, Los Angeles, CA, USA.

# Report Documentation Page

Public reporting burden for the collection of information is estimated to average 1 hour per response, including the time for reviewing instructions, searching existing data sources, gathering and maintaining the data needed, and completing and reviewing the collection of information. Send comments regarding this burden estimate or any other aspect of this collection of information, including suggestions for reducing this burden, to Washington Headquarters Services, Directorate for Information Operations and Reports, 1215 Jefferson Davis Highway, Suite 1204, Arlington VA 22202-4302. Respondents should be aware that notwithstanding any other provision of law, no person shall be subject to a penalty for failing to comply with a collection of information if it does not display a currently valid OMB control number.

| 1. REPORT DATE **NOV 1999** | 2. REPORT TYPE | 3. DATES COVERED **00-00-1999 to 00-00-1999** |
|---|---|---|

| 4. TITLE AND SUBTITLE | 5a. CONTRACT NUMBER |
|---|---|
| **A micromachined magnetic-field sensor based on an electron tunneling displacement transducer** | 5b. GRANT NUMBER |
| | 5c. PROGRAM ELEMENT NUMBER |
| 6. AUTHOR(S) | 5d. PROJECT NUMBER |
| | 5e. TASK NUMBER |
| | 5f. WORK UNIT NUMBER |

| 7. PERFORMING ORGANIZATION NAME(S) AND ADDRESS(ES) **Naval Research Laboratory,Code 6170,4555 Overlook Avenue SW,Washington,DC,20375** | 8. PERFORMING ORGANIZATION REPORT NUMBER |
|---|---|

| 9. SPONSORING/MONITORING AGENCY NAME(S) AND ADDRESS(ES) | 10. SPONSOR/MONITOR'S ACRONYM(S) |
|---|---|
| | 11. SPONSOR/MONITOR'S REPORT NUMBER(S) |

12. DISTRIBUTION/AVAILABILITY STATEMENT
**Approved for public release; distribution unlimited**

13. SUPPLEMENTARY NOTES

14. ABSTRACT
**We describe a micromachined magnetic-field sensor that is based on an electron tunneling transducer. This tunnel sensor is small, very sensitive, operates at ambient temperature and requires very little power. The measured resolution of the sensor is 0.3 nTr6Hz at 1 Hz. The limiting resolution, calculated based on fundamental noise sources, is 0.002 nTr6Hz at 1 Hz. The dominant source of the observed noise in the present device is low frequency air pressure fluctuations.**

15. SUBJECT TERMS

| 16. SECURITY CLASSIFICATION OF: | | | 17. LIMITATION OF ABSTRACT | 18. NUMBER OF PAGES | 19a. NAME OF RESPONSIBLE PERSON |
|---|---|---|---|---|---|
| a. REPORT **unclassified** | b. ABSTRACT **unclassified** | c. THIS PAGE **unclassified** | **Same as Report (SAR)** | **13** | |

**Standard Form 298 (Rev. 8-98)**
Prescribed by ANSI Std Z39-18

tunneling accelerometer has subsequently achieved a resolution of $10^{-8}$ g/$\sqrt{\text{Hz}}$ at 1 kHz [7,8]. The first tunneling magnetic-field sensor, reported by Wandass et al. [6], used a tunneling transducer to measure the elongation or contraction of a metallic glass ribbon in response to a change in the local magnetic field. The prototype sensor had a resolution of 2000 nT at 1 Hz. An improved version of the sensor reported by Brizzolara et al. [9], achieved a resolution of 6 nT/$\sqrt{\text{Hz}}$ at 1 Hz. However, the design proved to be better for measuring magnetostrictive strain [10,11] than low magnetic fields and was subsequently dropped in favor of the micromachined design presented in this paper.

Other micromachined sensors based on tunneling transducers have also been reported. Kenny et al. [12,13] demonstrated a miniature infrared detector that is similar to a golay cell except that a tunneling transducer is used to measure the deflection of the diaphragm that expands in response to the thermal expansion of a trapped gas. MacDonald and coworkers [14,15] and Jiang et al. [16] have fabricated micromachined silicon tip transducer arrays for various applications including tactile sensing. Kobayashi et al.[17] have utilized surface micromachining to construct an operational lateral tunneling sensor. Other tunnel sensor concepts for magnetic field [18,19], electric field, temperature [20], gravity, sound, pressure [21], strain, and chemical moiety have been proposed but not yet implemented. All of the micromachined tunnel sensors have resolutions at least equivalent to commercially available room temperature devices, but with significantly reduced volume, power, and potentially, cost.

Tunneling has also been employed to develop a novel force sensor, namely, the atomic force microscope (AFM) [22] with early application in the imaging of surfaces with high spatial resolution. Today, many AFM instruments have been sold to a growing nanometer-scale science and technology community with many diverse applications in biology, materials science, magnetics, tribology, adhesion, etc. From a sensing perspective, these force sensors have also been used to develop novel chemical and biochemical sensors that exhibit single molecule recognition capabilities [23,24].

In this paper, we describe a micromachined magnetic-field sensor. The device detects magnetic fields by sensing changes in torque on a suspended magnet. This sensor was designed with the objective of making a small, low-power, highsensitivity sensor that can be micromachined. We discuss the mechanical and electronic components of the sensor and address many issues associated with the performance of this and other tunnel sensors that operate at low frequency.

## 2. Experimental details

The sensor components are made using a bulk silicon micromachining process. A schematic diagram of the sensor is shown in Fig. 1 and photographs of the micromachined components are shown in Fig. 2. The sensor is built from a pair of micromachined components, that we call the "torsion element" and the "substrate".

The substrate is made from silicon (100) wafers that are 400 $\mu$m thick and have a diameter of 75 mm. The wafers are initially coated with 0.5 $\mu$m of oxide by steam oxidation at 1050°C for a period of about 45 min. One side of the wafer is patterned in a conventional positive resist process to expose the recess area, except for a 30-$\mu$m square that will be formed into the tip. The exposed oxide is etched until completely removed in a $CF_4$ reactive ion etcher (RIE), and the wafers are cleaned in acetone. An ethylene diamine pyrocatechol solution (EDP, also known as PSE 300 from Transene) is heated to 80°C in a reflux condenser (silicon nitride etching apparatus, Transene). The substrate wafer is submerged in this etching solution, which normally etches silicon (100) at about 50 $\mu$m/h under these conditions. After about 10 min, the wafers are removed from the solution, rinsed, and inspected by optical microscopy to investigate the progress of the formation of pyramidal tips at the locations of the 30 $\mu$m squares of protected oxide mask. The goal is to produce tips that are pyramidal with 1–3 $\mu$m diameter flat area on the end. To achieve this shape, several etch/inspection iterations are usually required. Typical yield is about 75%.

After formation of the tip is complete, the substrates are cleaned, stripped of all remaining oxide in a buffered HF solution, and inserted into the steam oxidation furnace for growth of 1.5 $\mu$m of $SiO_2$ (6 h at 1050°C). This oxide is stripped in HF, and then regrown once again. This grow/strip/grow sequence is used to intentionally round the end of the tip to a radius of curvature of at least 1 $\mu$m. Without this process, the edges of the flat area on the end of the tip occasionally have a slight overhang that introduces an open circuit between the metal deposited on the end of the tip and the metal leading to the bond pad.

After the second oxidation, the wafers are spin-coated with photoresist and patterned. Next, deposition of titanium (15 nm), platinum (15 nm) and gold (200 nm) is carried out in an e-beam evaporator. The wafers are then submerged in acetone to lift off the resist-coated regions and leave behind the patterned electrodes. The Ti and Pt layers are necessary for adhesion and diffusion barriers. This metal deposition process was selected as the best choice from several experiments with this and other metal deposition recipes [25]. After lift-off, the electrodes are coated with photoresist, and cut into individual substrates in a wafer dicing saw. The wafers are cleaned once again in TCE, acetone, and methanol. The wafers are then treated with an $O_2$ plasma to remove residual organic deposits.

The torsion element is made from silicon (100) wafers that are 125 $\mu$m thick and 50 mm in diameter. They are coated with 0.50 $\mu$m of $SiO_2$ by steam oxidation as above, patterned to expose the silicon between the frame and the
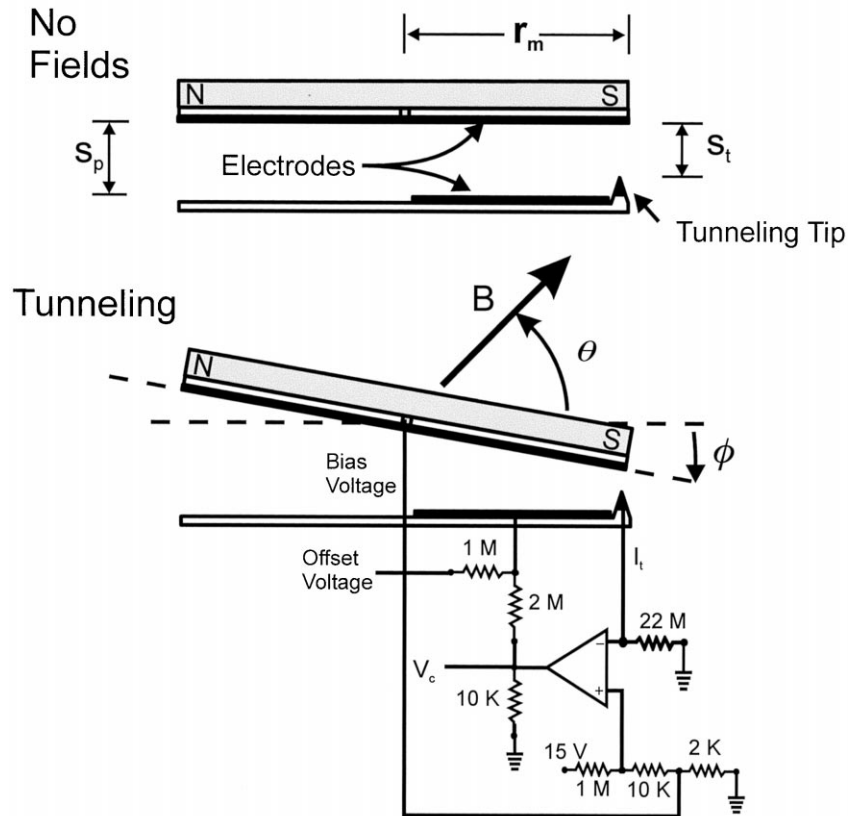
Fig. 1. Schematic diagram of the micromachined magnetic-field tunnel sensor (side view) and feedback control electronics. The upper view shows the orientation of the torsion arm with no magnetic or electric field present. The lower view shows the orientation during normal operation (i.e. tunneling).

torsion element, and leave behind a thin silicon torsion wire. This pattern must be accurately aligned to the crystal planes of the wafer to prevent undercutting of the thin wire during the anisotropic silicon etchant (EDP).
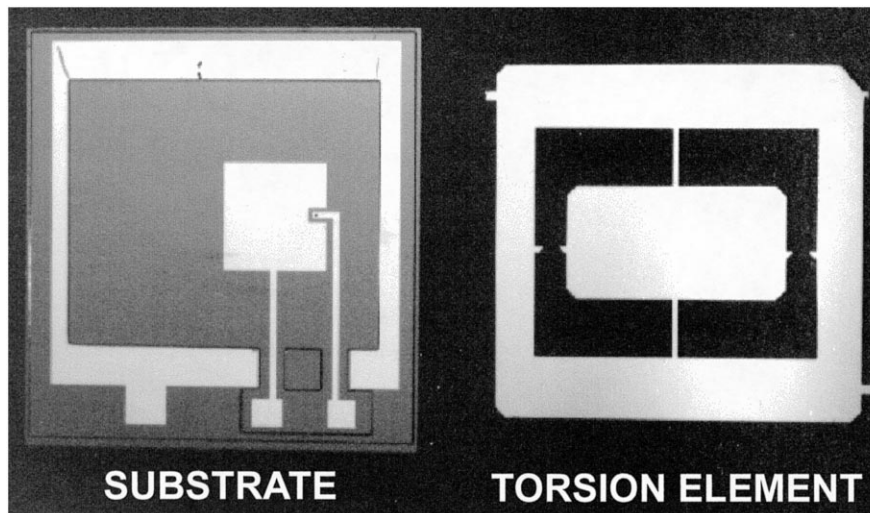


Fig. 2. Photograph of two silicon micromachined parts of the micromachined magnetic-field tunnel sensor. Each component is about $19 \times 19$ mm$^2$. The substrate, on the left, shows the configuration of the control electrode and tip (bottom part in Fig. 1). The part on the right is the torsion element that supports the magnet (top part in Fig. 1).

Each torsion element is etched in EDP until the exposed parts of the pattern are etched completely through the wafer. They are then removed from the etchant, cleaned in solvents, oxide stripped in a buffered HF solution, and inserted into the oxidation furnace for growth of a single 1.5-$\mu$m oxide layer. The insertion and removal of these elements from the furnace must be done very carefully, because there are extreme thermal gradients between the various parts of the wafer that can lead to thermal-expansion-induced breakage. After removal from the furnace, the wafers are coated on one side with the same metal layers as above. There is no patterning required on this part since the entire electrode is common in the transducer circuit.

An alternative process for the torsion element fabrication was used towards the end of the project when it was realized that sensor failures due to crushed tunneling tips were common. In the new design, the torsion element is modified to include a flexible landing pad at the position where the tip may come in contact with the counter electrode. The flexible pad is a 0.5-$\mu$m thick low-stress silicon nitride film. The fabrication process for these elements is modified as follows. The wafers are initially coated with the nitride film that will serve both as the flexible pad and as the etch mask. The first etch process opens a square window on one end of the torsion element. After etching, there is a 2-mm square diaphragm of nitride on the bottom of this window. The wafers are cleaned after etching, and then immediately coated with the metals on the diaphragm side of the wafer.

The fabrication process described above relies completely on low-resolution lithographic patterns. The masks used in this project were printed from postscript files to thin plastic sheets at a local printing house using a Linotronic printer. This printer has a resolution of 3380 dpi, which corresponds to a resolution of better than 10 $\mu$m. In fact, it is unwise to rely on feature dimensions below 20 $\mu$m from this process, but, within this constraint, decent patterns are available on 1-h turnaround at a cost of less than US$20. These plastic films are then transferred to lithographic masks by contact printing. Since none of the feature dimensions needed for this project were smaller than 35 $\mu$m, this approach is perfectly adequate, and offers substantial advantages with respect to the time needed to modify designs. The entire design/fab/build/test cycle for sensors made in this process was often shorter than 1 week! Our impression of this process for tunnel sensor fabrication is that it is remarkably simple to carry out. We strongly encourage all researchers interested in tunnel sensor research projects to build some simple devices by a process similar to the one described here before undertaking a more complicated process development sequence. The sensors built in this process can serve as a platform for materials and control-system testing in parallel with the later process development. And sensors built in this process can help emphasize the elements of the final process

that are absolutely essential to tunnel sensor operation — electrode cleanliness, electrode isolation, tip crash survival, and control-system behavior — all of which cannot be characterized by optical or SEM images of the device.

An assembled device is shown in Fig. 3. In the assembled device, the rectangularshaped support suspended from the torsion beams has a magnet attached on the side facing the page and a vapor-deposited gold electrode on the opposite side. A sensor is assembled by manual attachment (epoxy) of a permanent magnet to the torsion element followed by placement of the torsion element on top of the substrate. The parts are mechanically clamped together, and then bonded around the perimeter with epoxy. In some cases, the micromachined components are treated before final assembly by immersion in a 1-mM solution of dodecane thiol ($C_{12}H_{26}S$) for 2 to 4 days. This treatment produces an ordered self-assembled thiol monolayer on the gold surfaces [26] and this monolayer helps to reduce the adhesive interaction between the gold electrodes.

The following experiment was done to determine the dipole moment of the magnet. A sample holder that held a suspended magnet and could be mounted in an STM was built. The sample holder was a ceramic (Macor) disk with a 25-mm diameter, 5 mm thick. The disk had a 10-mm diameter hole in the center and a 50-$\mu$m-diameter tungsten wire was strung tightly over the hole. The wire was tied down at points on either side of the hole. A small magnet ($1 \times 0.9 \times 9$ mm$^3$) similar to those used in the sensors was coated with a thin layer of sputter-deposited gold. The
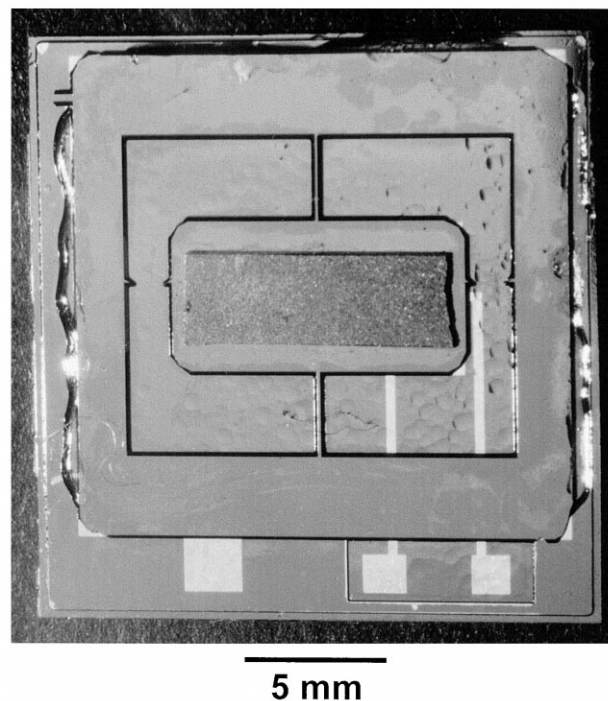


**5 mm**

Fig. 3. Photograph of the assembled micromachined magnetic-field tunnel sensor.

magnet was attached to the tungsten wire with silver epoxy so that the wire bisected its long axis. When the sample holder was mounted in the STM, the long axis of the magnet was oriented perpendicular to the test magnetic field. A 38-nm deflection was observed when 26-nT test field was applied. The tunneling tip was positioned near the end of the magnet approximately 4.5 mm from the pivot point.

The magnetic dipole was calculated to be 0.013 A m$^2$ based on the rotation of the magnet and on the geometry and physical properties of the tungsten wire. To do the calculation, the wire was treated as a cylindrical bar with a length of 1 cm. The angle of twist for a torque applied at the center of the bar is given by $\phi = (8L\tau)/(D^4\pi G)$ where $L$ is the length of the bar, $\tau$ is the torque, $D$ is the diameter of the bar and $G$ is the shear modulus for tungsten $(1.6 \times 10^{11}$ N m$^{-2})$. The dipole, $m$, is calculated from $m = \tau/B$. The calculated dipole has an estimated uncertainty of approximately 50% based on the uncertainty in the STM calibration (10%), the uncertainty of the applied field (10%) and on the uncertainties of the geometric parameters (cumulative 30%).

A custom-made testing station was built for the tunnel sensor. The testing station includes a Lucite block with a shallow well to hold the sensor. The sensor is mounted in the well with its plane parallel to the table top. Placing the sensor in the well permits immersing the sensor in fluid if desired. When mounted, the tunnel sensor is at the midpoint of the axis of a 10-cm diameter Helmholz coil. All measurements were made in a degaussed magnetically shielded chamber (Schoensted Model S66) that was optimally oriented with respect to the local magnetic field on the top of a vibration isolation table. The DC level of the residual field inside the degaussed chamber is given by the manufacturer as 1 nT. Noise spectra of the tunneling current and various voltages were measured with an FFT spectrum analyzer (Stanford Instruments Model SR 760).

## 3. Description of tunnel sensor

The schematic diagram for the sensor is shown in Fig 1. The device is built from the two micromachined silicon components described above and shown in Fig. 2. A photograph of the assembled sensor, including the magnet, is shown in Fig. 3. The electrode on the torsion element serves both as the tunneling counter electrode and as one of a pair of rotation control electrodes. The moving parts, including the magnet will be referred to below as the magnet assembly. The substrate (the part on the left in Fig. 2), includes the tunneling tip and the other rotation control electrode, both of which are on the bottom face of the 80-μm deep rectangular depression. Physical dimensions and properties for the sensor are listed in Table 1.

The thickness of the torsion beams insures that the rotation of the magnet assembly about the long axis of the

Table 1
Device specifications

| Length of magnet | 0.009 m |
|---|---|
| Width of magnet | 0.004 m |
| Thickness of magnet | 0.0005 m |
| Magnet | neodymium–iron–boron ($\sim$ 150 mg) |
| Area of electrodes, $A$ | $2.5 \times 10^{-5}$ m$^2$ |
| Torsion arm length, $r_m$ | 0.005 m |
| Length of torsion beams | 0.003 m |
| Thickness of torsion beams | 125 μm |
| Width of torsion beams | 180 μm |
| Shear modulus of silicon | $4 \times 10^{10}$ N m$^{-2}$ |
| Initial electrode gap, $s_p$ | 70 μm |
| Distance magnet moves to tunnel, $s_t$ | 25 μm |

beams is, by far, the mechanical mode with the lowest frequency. Only this mode is assumed to be important for the description of the performance of the sensor. The asymmetrical placement of the lower rotation control electrode leads to an electrostatic torque when there is a voltage difference between the control electrodes. When the feedback control circuit (see Fig. 1) is first powered, the gap between the electrodes is large and the tunnel current is much lower than the reference current. As a result, a control voltage, $V_c$, is generated and applied to the lower rotation control electrode. The torque resulting from the voltage difference between the electrodes causes the magnet assembly to rotate about the long axes of the torsion beams and reduces the tunneling gap. The rotation continues until the tunneling gap is set to give the desired tunneling current. Once the desired tunneling current is established, there is no change in the voltage applied to the electrode unless the local magnetic field changes. For small magnetic field changes the *feedback control circuit adjusts the control voltage quickly enough that the magnetic assembly does not move significantly*. The feedback control circuit used to establish and maintain tunneling is similar to one reported previously [1]. For the circuit shown in Fig. 1, the tunnel current, $I_t$, is set to 1.3 nA and the tunnel bias, $V_{bias}$, to 0.18 V. Because the control voltage from the feedback controller, $V_c$, is limited to $\pm 15$ V, an offset voltage, $V_0$, is needed to establish a tunnel current. The voltage on the control electrode when the device is tunneling is $V_t = V_c + V_0$. If power is applied, the magnet assembly is always rotated so that it is within tunneling distance of the tip. For this device the electrostatic torque needed to rotate the magnet assembly into tunneling range is balanced by the mechanical restoring torque due to the stress in the beams and by the magnetic torque due to the local magnetic field acting on the magnet. In order to quantify the electrostatic torque, the rotation control electrodes can be approximated as a parallel plate capacitor [27] since the geometry of the device is selected to ensure that the control electrodes are always

nearly parallel. The force between the plates of a parallel plate capacitor is

$$F = \frac{\kappa \varepsilon_0 V^2 A}{2 s_0^2} \tag{1}$$

.

Taking into account the torque balance associated with electrostatic, mechanical and magnetic components, the voltage on the control electrode needed to establish tunneling is

$$V_t = \sqrt{\frac{2 \tau_{\mathrm{opposing}} s_0^2}{\kappa \varepsilon_0 r_e A}} \tag{2}$$

where the torque opposing the electrostatic torque is $\tau_{\mathrm{opposing}} = k_t \phi_0 - m(B_0 \sin \theta_0 + B_1 \sin \theta_1)$. $k_t$ is the mechanical torque constant, $\phi_0$ is the angle that the magnet assembly makes with the zero mechanical torque position, $m$ is the magnetic dipole of the magnet, $B_0$ and $B_1$ are the static and test magnetic fields, $\theta_0$ and $\theta_1$ are the angles these fields make with the magnetic dipole, $s_0$ is the average electrode spacing when the device is tunneling, $\kappa$ is the dielectric constant for the medium between the electrodes, $r_e$ is the moment arm for the electrostatic torque, $A$ is the area of the electrodes, and $\varepsilon_0 = 8.85 \times 10^{-12}$ f/m. Note that $\sin \theta_0$ and $\sin \theta_1$ can be positive or negative. The value of $r_e$ is approximated as one quarter of the length of the magnet assembly. From the geometry of the device, the control electrode separation when the device is operating and at equilibrium is $s_0 = s_p - s_t/2$, where $s_p$ is the distance between the rotation control electrodes when no fields are present and $s_t$ is the distance between the tunneling electrodes when no fields are present. The distances $s_p$ and $s_t$ are illustrated in the upper part of Fig. 1. Also, from the geometry of the device, the angle that the magnet makes with the zero mechanical torque position is $\phi_0 = s_t/r_m$, where $r_m$ is defined in Fig. 1. Note that the tunneling gap is negligible compared to $s_p$ and $s_t$. In general, $V_t$ will depend on the orientation of the sensor with respect to the local magnetic field since the magnetic torque may be significant compared to the mechanical torque.

The torque produced by the electrostatic force scales as the square of $V_t$. Since the offset voltage is generally more than an order of magnitude larger than the control voltage, the square of this voltage sum is dominated by the square of the offset voltage. The next largest term arises from the cross-term in the product, which is linearly dependent on the control voltage. The term that depends on the square of the control voltage may be neglected. As a result, variations in the rebalance torque applied to the torsion element are proportional to the variations in the control voltage, which may be recorded as signal.

Assuming constant electrode separation, $s_0$, and that the change in torque due to magnetic field variations makes a small contribution to the opposing torque, the sensitivity $(V/T)$ for the sensor is

$$\frac{dV_t}{dB} = \sqrt{\frac{m^2 s_0^2 \sin^2 \theta_1}{2 \kappa \varepsilon_0 r_e A \tau_{\mathrm{opposing}}}} \tag{3}$$

.

## 4. Results

### 4.1. Sensitivity and $V_t$

Calculated values for sensitivity and $V_t$ are given in Table 2 and compared to the ranges of values measured for about 50 sensors. The device specifications given in Table 1 are used in these calculations. $\theta_1$ is 90° and $\boldsymbol{B}_0$ is assumed to be zero since the measurements are made in a shielded chamber. The value of the mechanical torque constant, $k_t$, is calculated for a beam of rectangular cross-section.

The calculated value for $V_t$ is at the high end of range of 80–330 V that was observed for the sensors. The large variation in the operating voltage is due to our present inability to control fabrication accurately enough to ensure consistent tip height and electrode spacing. The calculated field sensitivity also falls within the range observed. However, the measured sensitivity is typically higher than the calculated value. The less than perfect agreement can be partly explained by differences between the assumed and actual geometry. For example, the electrostatic torque is calculated for parallel electrodes but this assumption is only approximately true for the sensor when it is in operation. Also, the effective torque constant for rotation of the magnet assembly, $k_t$, is calculated by assuming beams of rectangular cross-sectional area when in fact the torsion beams have a trapezoidal cross-section as a result of the etching process. The size of the magnetic dipole will also play an important role; we did not precisely control the size of the magnet for different sensors and the dipole moment was only measured for one magnet. Finally, the model is based on several assumptions that may underestimate the sensitivity. For example, the non-linearities in the electrostatic force and non-torsional motions of the structure have been neglected.

### 4.2. Frequency response

The frequency response was measured for several devices. Most devices were tested in air but a few were

Table 2
Performance parameters

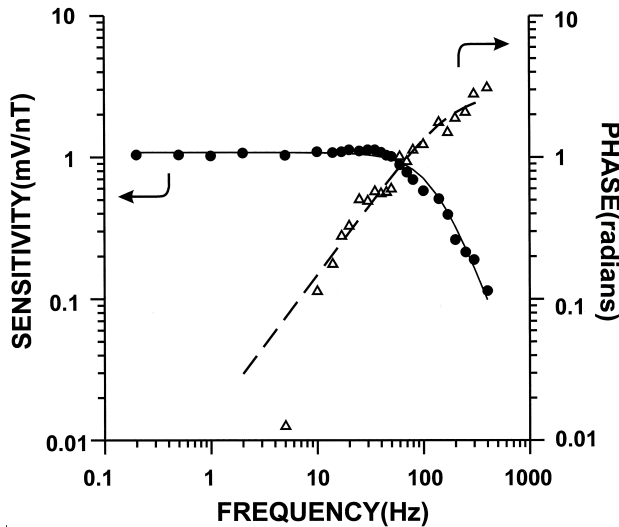| Parameter | Calculated ($B_0 = 0$) | Observed |
|---|---|---|
| Voltage on control electrode, $V_t$ | 289 V | 80–330 V |
| Field response, $dV_t/dB$ | 0.56 mV/nT | 0.5–3 mV/nT |
| Resonant frequency, $f_0$ | 169 Hz | 80–125 Hz |
| $B_{\mathrm{max}}$ | 224,000 nT | not determined |

Fig. 4. Plot of the measured and fitted frequency response and phase data for a micromachined magnetic-field tunnel sensor in air. The circles and triangles are the measured frequency response and phase shift, respectively. The solid and dashed lines are the corresponding fitted curves.

### 4.3. Voltage required for tunneling

The voltage needed on the control electrode to establish tunneling, $V_t$, varied from 80 to 330 V. This wide range is not surprising because there are large variations in the tip height and in the flatness of the wafers used to fabricate the devices. As can be seen from Eq. 1, $V_t$ depends strongly on the average equilibrium spacing between the rotation control electrodes ($s_0$,), the torque constant ($k_t$) and the angle through which the magnet assembly must rotate to establish tunneling ($\phi_0$). It is interesting to note that $V_t$ is sometimes observed to vary by a factor of two for a given device when the two parts are shifted laterally relative to each other before the epoxy is applied. This variation indicates that greater control over the flatness of the wafers is needed. A possible solution to this problem is discussed below.

### 4.4. Resolution vs. $V_t$

The model proposed above for the operation of the sensor is valid as long as the tunneling gap remains constant. An alternate equation for the voltage sensitivity indicates that it should depend on $V_t$ if this model is correct.

$$\frac{dV_t}{dB} = \frac{ms_0^2 \sin \theta_1}{A \kappa \varepsilon_0 r_e V_t} \tag{4}$$

According to Eq. (4), a plot of log(sensitivity) vs. log($V_t$) should have a slope of $-1$. According to Eq. (2), $V_t$ depends on the geometry of the device and on the magnitude of the local magnetic field. The geometry of a given device cannot be changed, but $V_t$ can be varied by changing the position of a strong magnet located near the tunnel sensor. The plot in Fig. 5 shows the experimentally determined variation of the sensitivity as a function of $V_t$. The

tested while immersed in a viscous fluid (DOW 704 diffusion pump oil). Tests for devices under oil were made because we anticipate that these devices may be more robust when immersed in a viscous fluid. The frequency response and phase shift were determined by applying a known magnetic field that was generated by the Helmholz coil. The amplitude and phase of the control voltage, $V_c$, were measured using a digital oscilloscope. Fig. 4 shows typical data for a device in air.

Phase shift and frequency response data were simultaneously fitted to the appropriate harmonic oscillator equations, using the Marquardt–Levenberg algorithm provided with SigmaPlot 4.01. Three parameters were allowed to vary: amplitude, the resonant frequency, $f_0$, and $Q$. The resonant frequency was constrained to fall between 0 and 400 Hz and $Q$ was constrained to fall between 0.01 and 50. For the data shown in Fig. 4 the fitting procedure produces the values $Q = 0.53$ and $f_0 = 125$ Hz. To verify reproducibility, three different sets of data for the same device were fitted. For a typical device $Q$ varied by $\pm 5\%$ and $f_0$ by $\pm 25\%$. The $Q$ associated with the measured response of this device is reduced by the feedback control system, which acts to cancel excursions from the desired torsion element position. As a result, the measured $Q$ is substantially less than the values of 50 or so that would be expected for an open loop system of this geometry operating in air [28]. The frequency responses for devices measured in oil are similar except that the roll-off frequency is much lower, typically around 2 Hz instead of 20 Hz. Typical $Q$ values were lower, usually between 0.2 and 0.4. This lower value of $Q$ is expected because of the increased viscous damping associated with the oil between the electrodes.
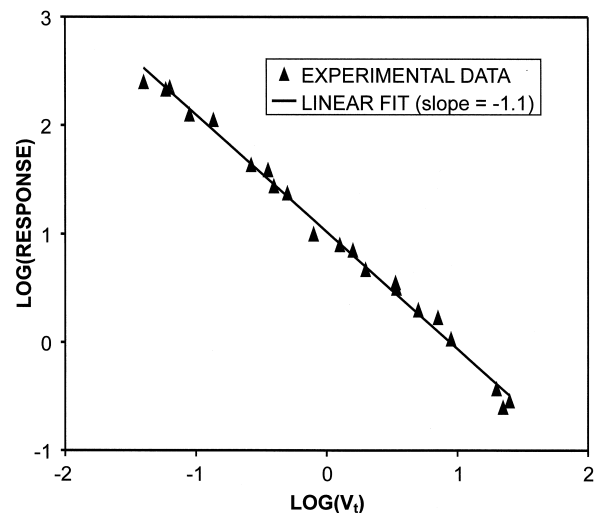


Fig. 5. Plot of the magnetic field sensitivity vs. $V_t$, the voltage needed to establish tunneling.

observed slope of the log–log plot is very close to predicted value of $-1$ as expected from the model.

## 5. Noise analysis

### 5.1. Fundamental noise

Johnson, shot and thermal noise are intrinsic and irreducible in any given device and set a lower limit on the voltage noise. The thermal, or Brownian, noise in the mechanical modes of a macroscopic system is not significant and shot and Johnson noise are the limiting sources of fundamental noise. On the other hand, thermal noise can be significant in a micromachined tunnel sensor because of the small masses involved and the high displacement sensitivity of the tunneling displacement transducer. For our sensors the thermal mechanical noise always dominates Johnson and shot noise.

According to the equipartition theorem, each mode of a mechanical system at equilibrium has an average thermal noise energy of $k_B T/2$ for each quadratic term in the energy expression for that mode [29]. The most important mechanical mode for this sensor is the torsional mode since it is the only one that when excited has a significant effect on the tunneling gap and tunneling current. Following the treatment given by Gabrielson [29] for an accelerometer, it can be shown that the signal-to-noise ratio for the device, if limited by thermal noise, is given by,

$$\text{SNR} = m\Delta B \sin\theta_1 \sqrt{\frac{Q}{4 k_B T \sqrt{k_t J}}} \qquad (5)$$

where SNR is the signal-to-noise ratio (unit: $\text{Hz}^{-0.5}$), $k_B$ is Boltzman's constant, $T$ is absolute temperature, $k_t$ is the

torque constant, $Q$ is the quality factor and $J$ is the moment of inertia of the rotating element. Note that $k_t$ has contributions from mechanical, magnetic, and electrostatic sources, but is typically dominated by the mechanical contribution.

Fig. 6 illustrates the measured and theoretical resolution ($\text{nT}/\sqrt{\text{Hz}}$) of the device. Four quantities are plotted vs. frequency in the Fig. 6 These are, the measured sensitivity (in $\text{mV}/\text{nT}$), the calculated sensitivity (in $\text{mV}/\text{nT}$), from Eq. (3), the sensor noise in air measured with no applied magnetic field (in $\text{mV}/\sqrt{\text{Hz}}$) and the calculated fundamental noise (in $\text{mV}/\sqrt{\text{Hz}}$). The calculated noise is the lowest noise that is possible based on fundamental sources (Johnson, Brownian and shot).

Fig. 6 was constructed so that the measured noise can be readily compared to the fundamental noise. As indicated in Eq. (4), the signal-to-noise ratio is constant for a given device if the only source of noise is fundamental noise. For Fig. 6, this fact was used to normalize the calculated response so that the calculated fundamental noise could be properly positioned on the chart. As discussed above, the magnitude of the calculated sensitivity does not usually agree with the measured sensitivity particularly for those sensors that show high response. The resolution of the device based on the experimental data is 0.3 nT $/\sqrt{\text{Hz}}$ at 1 Hz. Similar results were obtained for devices in oil.

### 5.2. Excess noise

In addition to the fundamental noise discussed above, real devices have various sources of excess noise that can be eliminated in principle but, in practice, often set the noise limit for a device. As can be seen in Fig. 6, the noise
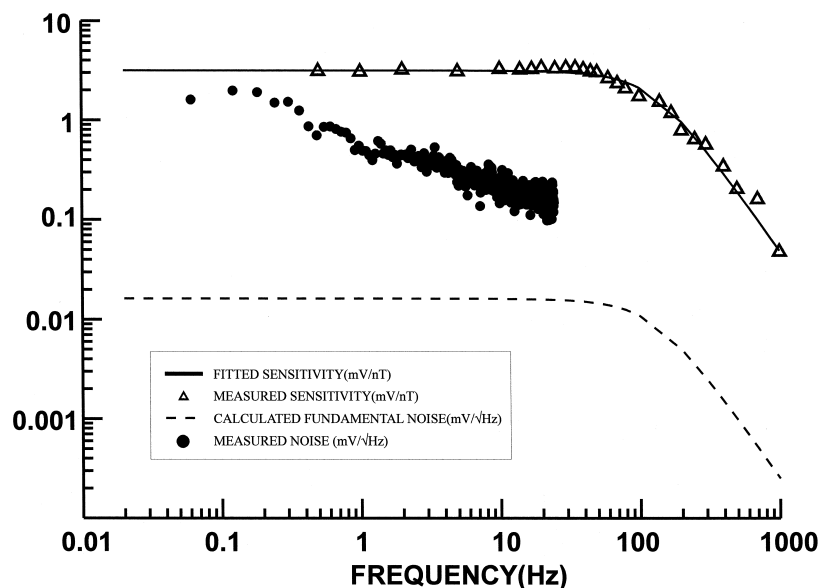


Fig. 6. Plot of the measured field sensitivity, calculated field sensitivity, measured noise, and fundamental noise for a micromachined magnetic-field tunnel sensor. The calculated field sensitivity has been normalized to the measured field sensitivity.
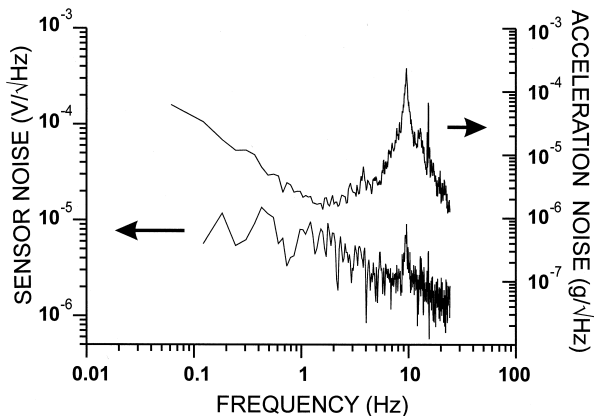
Fig. 7. Comparison of platform noise and tunnel sensor noise as a function of frequency.

level measured for the tunnel sensor is more than an order of magnitude greater than the level expected from fundamental noise. It is also notable that the shape of the observed noise spectrum is considerably different from that predicted based on fundamental noise sources.

There are many possible sources for the excess noise in these devices including differential thermal expansion leading to lateral drift of the tip relative to the counter electrode, mechanical drift due to instability or curing of the epoxy, migration of gold surface atoms, drift in the magnitude of the magnetic dipole, electrode surface contamination, and differential responses of various mechanical components to external accelerations or air pressure fluctuations. Some of these noise sources are easily evaluated from experiments but others are difficult to quantify.

The dipole moment of the magnet is temperature dependent. The noise generated by a changing dipole is directly

proportional to the average value of the local field. The importance of this noise can be gauged by observing the noise for a sensor with and without magnetic shielding. For these devices, there is no observable increase in low frequency noise when the sensor is outside the shielded chamber, and therefore, dipole drift noise does not contribute significantly to the measured noise.

Platform vibration noise was measured with an accelerometer mounted on the table that held the sensor testing station. The table has a strong resonance at 8 Hz that is useful for gauging the sensitivity of the sensor to platform vibrations. Fig. 7 shows both the acceleration noise for the table and the sensor noise. For these data, the sensitivity to vibration noise was determined to be 4 $\mu$V /$\mu$g and other than the 8-Hz peak, the vibration noise does not contribute significantly to the observed noise. It should be noted that the 8 Hz peak was often much smaller or not seen at all in the noise spectra of the tunnel sensors. This peak is expected to correlate with an imbalance of the mass of the magnet on the two sides of the torsion beams.

We have long been aware that environmental pressure fluctuations can apply forces to the torsional element. For this sensor, there is a volume of air between the torsion element and substrate that can escape to the surroundings only along the edges. When the external pressure changes suddenly, there is a net force on the torsion element until the pressure re-equalizes. During studies of the noise in these structures, it became clear that building pressure fluctuations due to airflow in the room or openings and closings of doors were correlated with many of the noise signals being recorded.

The following experiment was done to gain a better understanding of the effects of ambient air pressure fluctu-
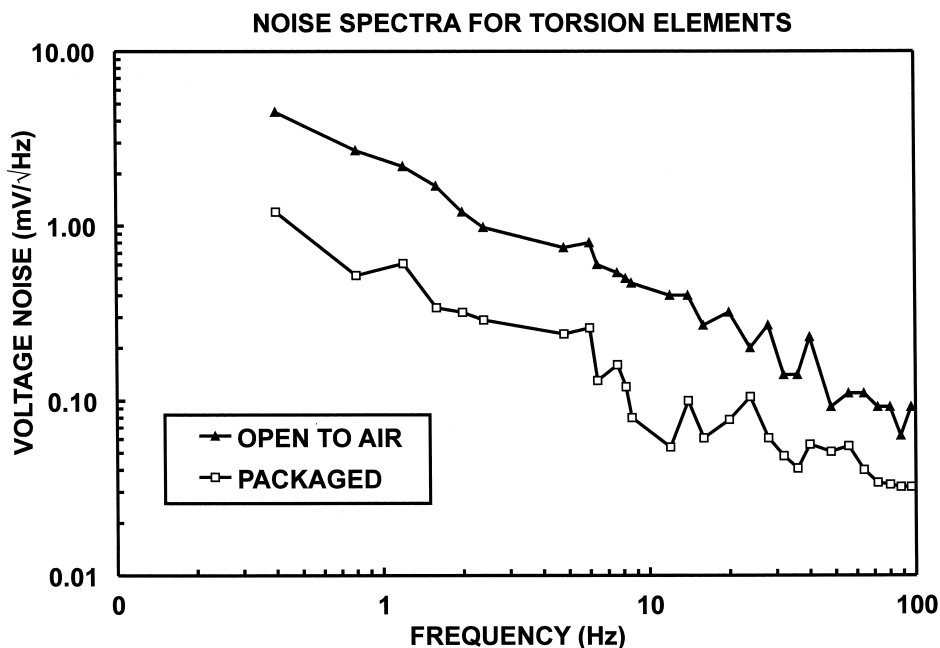


Fig. 8. Comparison of noise spectra measured before and after packaging to reduce pressure fluctuation in the room air.

ations on the behavior of the sensors. A device was thoroughly characterized before and after hermetically sealing it in a small, stiff package. Before sealing, the device was calibrated with an optical interferometer, which allowed experimental determination of the relationship between deflection voltage and torsion element deflection. A spectrum analyzer was used to record the voltage noise spectrum shown as the upper curve plotted in Fig. 8. The same device was then sealed in a hermetic package by epoxying a silicon lid onto the structure and sealing the perimeter with more epoxy. Immediately upon the formation of the seal, the noise spectrum of this device was substantially reduced. A noise spectrum recorded after sealing the sensor is shown as the lower trace in Fig. 8. As is seen, the noise recorded after the formation of the seal is approximately five times smaller than that for the unsealed device. These observations are consistent with previously observed improvements in the behavior of other tunnel sensors with hermetic packaging [7,8,12,13]. It is clear that air pressure fluctuations are the dominant source of the observed noise in the magnetic-field sensors, and that improved sensor packaging is the most promising approach for improving sensor performance. Based on the experiment described above, it is clear that performance improvements on the order of five times may be achieved with better packaging.

## 6. Discussion

The resolution $(0.3 \text{ nT}/\sqrt{\text{Hz}})$ achieved with this device is quite good especially when comparing its size and power consumption to other magnetic-field sensors as shown in Table 3. It should be possible to achieve better performance since the noise level can be reduced with better packaging as noted above. Once the pressure fluctuation noise is lowered, other sources may dominate. Several other sources of excess noise were mentioned above. We will now consider some of these noise sources in more detail and propose strategies for reducing their magnitudes.

Table 3
Comparison of magnetic-field tunnel sensor to related sensors

| Type | Resolution $(\text{nT}/\sqrt{\text{Hz}})$ | Volume $(\text{cm}^3)$ | Power $(\text{mW})$ |
|---|---|---|---|
| SQUID (at 4 K) | $10^{-6}$ | 10 | 1000 |
| Fiber optic | $7 \times 10^{-5}$ | 60 | 500 |
| Optically pumped | $10^{-3}$ | 500 | 7500 |
| Tunneling[a] | $2 \times 10^{-3}$ | 10 | 1 |
| Proton precession | $10^{-2}$ | 500 | 1000 |
| Fluxgate | $3 \times 10^{-2}$ | 50 | 500 |
| Magnetotransistor | 10 | 1 | low |
| Hall probe | 1000 | 5 | 100 |
| Magnetodiode | 1000 | 1 | low |
| Magnetoresistor | 1000 | 1 | low |

[a] Projected resolution.

Lateral thermal drift is similar in effect to a tip scanning the surface of the counter electrode as in scanning tunneling microscopy. Atomic force and scanning tunneling microscopy images of the evaporated gold surfaces of the electrodes show a faceted structure with facet diameters of about 50 nm and facet heights of 5–10 nm. Computer modeling of the tunneling current that is expected as a result of lateral drift of a tunneling tip over a surface of this type shows that this noise source is unlikely to account for the observed noise unless the surfaces are moving at least 1 nm/s relative to each other. This rate is a couple of orders of magnitude higher than that expected, based on typical scanning tunneling microscopy data. Of course the drift might be faster in these devices and reduction of the pressure fluctuation noise might result in this drift noise, making a significant contribution. There are at least two ways to reduce noise resulting from lateral drift of the tunneling tip. First, the sensor is designed to minimize thermal gradients. Both the materials used to construct the device (mostly silicon in this case) and the method of device construction are important. The present devices are assembled using epoxy that is subject to creep. Assembly using silicon bonding techniques would eliminate creep as a potential source of noise. Second, attempts can be made to generate flatter electrode surfaces. Recently investigators in Belgium were able to deposit very flat gold films by raising the pressure in the deposition chamber to $5 \times 10^{-4} \text{Pa}(\text{O}_2 \text{ or He gas})$ [30].

Scanning tunneling and atomic force microscopy studies have shown that the atoms on a gold surface have a significant mobility, even at room temperature [31,32]. Passage of a gold atom under the tunneling tip or transfer of an atom to or from the tip can easily be detected in a tunnel sensor and these processes could contribute to the noise observed. This noise source is not easy to quantify. A possible solution to the problem of mobile surface atoms is the use of metal film electrodes that are made from a metal or alloy that has a lower surface atom mobility than gold. However, the choices of electrode material are limited by the electrical characteristics required for good tunneling junctions and by the requirements of relative simplicity for an inexpensive microfabrication process. A limited number of experiments for sensors with platinum electrodes gave noise spectra very similar to those for the gold electrodes.

A second solution to the problem of mobile surface atoms is the immobilization of the gold surface with an adsorbed monolayer. Thiol molecules are known to form self-assembled monolayers on gold surfaces and there is evidence that they do in fact stabilize the surface [33]. The thiols under consideration are long-chain hydrocarbons with the characteristic –SH group on one end. The thiols that form good self-assembled monolayers typically have fairly long linear hydrocarbon chains (e.g., $\text{C}_{12}\text{H}_{25}\text{SH}$ to $\text{C}_{18}\text{H}_{37}\text{SH}$). These monolayers are typically made by exposing the clean gold surfaces to thiol solutions in ethanol.

This treatment may have other benefits as well. Because of the adhesion of clean gold surfaces, noise can also occur as the result of the gold tip coming in contact with the gold counter electrode. For clean gold, the adhesive interaction can lead to material transfer from one electrode to the other. After contact between the electrodes, the tunneling current is likely to be noisier than usual until the electrode surfaces stabilize. Self-assembled thiol films on gold have also been shown to significantly reduce this adhesive interaction [34]. Finally, self-assembled thiol films may also help to protect electrode surfaces from the buildup of surface contamination layers. We have done some preliminary experiments with devices that had thiol-treated electrodes but the dominance of the pressure fluctuation noise made the noise improvement difficult to evaluate.

Most of the excess noise sources of excess noise discussed above will add noise to the tunneling current. If the tunneling current noise has a frequency component that falls within the bandwidth of the sensor, noise will appear on the control voltage. If this excess noise is the dominant source of noise, the signal-to-noise ratio is

$$\text{SNR} = \frac{mk_t r_m A\sqrt{\psi}\,G(f)\,\Delta B \sin\theta_1}{\ln\left(1 + \dfrac{\Delta I(f)}{I_0}\right)} \tag{6a}$$

where $\psi$ is the tunneling barrier height, $\Delta I$ and $I_0$ are the tunneling current noise and current (for gap $z_0$), respectively, and $G(f)$, the frequency response of a harmonic oscillator is

$$G(f) = \frac{1}{\sqrt{\left(1 - \dfrac{f^2}{f_0^2}\right)^2 + \dfrac{f^2}{f_0^2 Q^2}}} \tag{6b}$$

. This expression is frequency dependent, unlike the SNR derived for fundamental noise. In this case, the frequency response of the noise does not have the same shape as signal response.

If $\Delta I(f)$ is reduced to the lowest practical level, the signal-to-noise ratio can be optimized by maximizing the product $m\kappa_\tau \rho_\mu A\psi$. There are compromises, however. Increasing $k_t$ results in a larger value of $V_t$ and increasing $r_m$ or $A$ results in a larger device with a lower resonant frequency. For a given magnetic material, the dipole moment, $m$, can be made larger only at the cost of increased mass and to a lower resonant frequency and a greater susceptibility to tip damage. It is possible to have a large value for $k_t$ without increasing the $V_t$ if the distance between the electrodes during tunneling, $s_0$, is reduced (see Eq. (2)). The resulting device would have many advantages, including good signalto-noise ratio, a high resonant frequency and a reasonable value of $V_t$. With the

present bulk micromachining techniques that we use, it is difficult to reproducibly make devices with small values of $s_0$ because it is hard to fabricate the very flat electrodes required. However, it should be possible to routinely achieve much smaller values for $s_0$ by using surface micromachining techniques [17], and application of these methods to this device is under investigation.

Finally, it is worth noting a few practical considerations for the dynamic range. The dynamic range of this sensor, for fields that cause the magnet to rotate away from the tip, is determined by the voltage supply available. The dynamic range for fields that cause the magnet to rotate toward the tip is determined by the geometry of the device and the magnitude of the dipole. The electromagnetic torque is available only in one direction and if the device is in a strong field it may not be possible to prevent the electrodes from coming into contact. Eqs. (6a,6b) gives the maximum measurable field in this case.

$$B_{\max} = \frac{k_t \phi_0}{m} = \frac{k_t s_t}{m r_m} \tag{7}$$

If the product $k_t s_t$ is small, the torque on the magnetic dipole from the Earth's field may be large enough to force the magnet to rotate into contact with the tip. On the other hand if this product is very high, the voltage needed to achieve tunneling can be so great that the sensor may not be practical for many applications. For the device summarized in Table 1, the calculated value of $B_{\max}$ is 224,000 nT, a value that is safely above the average value of the Earth's field, 50,000 nT. One way to eliminate the dynamic range asymmetry is to build a device with a second control electrode. The second electrode is placed symmetrically on the opposite side of the torsion beams and can be used to pull the magnet away from the tip if necessary. This addition would lead to a increase in microfabrication and electronic complexity.

## 7. Summary

We have designed and fabricated a micromachined magnetic-field tunnel sensor. The tunnel sensor consists of two parts micromachined separately from silicon and then sandwiched together to form the sensor. One part includes the tunneling tip and control electrode, and the other part includes a rotatable element that supports the magnet. The tunnel sensor has achieved a demonstrated resolution of 0.3 T/√Hz at 1 Hz and has a predicted resolution limited by thermal noise of 0.002 nT/√Hz at 1 Hz. The measured noise level of the sensor exceeds that expected from fundamental noise sources and we have determined that low frequency air pressure fluctuations are a dominant source. Better device packaging should reduce the sensor noise by a factor of five. The micromachined tunnel sensor

has two other attractive attributes: it requires relatively little power compared to other sensors which similar performance and it should be fairly inexpensive if manufactured in large quantities.

## Acknowledgements

## References

[1] T.W. Kenny, W.J. Kaiser, J.A. Podosek, H.K. Rockstad, J.K. Reynolds, E.C. Vote, Micromachined tunneling displacement transducers for physical sensors, J. Vac. Sci. Technol., A 11 (1993) 797–802.

[2] M.F. Bocko, K.A. Stephenson, R.H. Koch, Vacuum tunneling probe: a nonreciprocal, reduced-back-action transducer, Phys. Rev. Lett. 61 (1988) 726–729.

[3] M.F. Bocko, K.A. Stephenson, Tunneling transducers: quantum limited displacement monitors at the nanometer scale, J. Vac. Sci. Technol., B 9 (1991) 1363–1366.

[4] M. Niksch, G. Binnig, Proposal for a novel gravitational-wave sensor, J. Vac. Sci. Technol., A 6 (1988) 470–471.

[5] S.B. Waltman, W.J. Kaiser, An electron tunneling sensor, Sens. Actuators 19 (1989) 201–210.

[6] J.H. Wandass, J.S. Murday, R.J. Colton, Magnetic field sensing with magnetostrictive materials using a tunneling tip detector, Sens. Actuators 19 (1989) 211–225.

[7] T.W. Kenny, S.B. Waltman, J.K. Reynolds, W.J. Kaiser, Micromachined silicon tunnel sensor for motion detection, Appl. Phys. Lett. 58 (1991) 100–102.

[8] H.K. Rockstad, T.W. Kenny, J.K. Reynolds, W.J. Kaiser, T.B. Gabrielson, A miniature high-sensitivity broad-band accelerometer based on electron tunneling transducers, Sens. Actuators A 43 (1994) 107–114.

[9] R.A. Brizzolara, R.J. Colton, M. Wun-Fogle, H.T. Savage, A tunneling-tip magnetometer, Sens. Actuators 20 (1989) 199–205.

[10] R.A. Brizzolara, R.J. Colton, Magnetostriction measurements using a tunneling-tip strain detector, J. Magn. Magn. Mater. 88 (1990) 343–350.

[11] R.A. Brizzolara, R.J. Colton, The magnetostriction of CoFeNiMo metallic glasses measured with a tunneling transducer, J. Magn. Magn. Mater. 103 (1992) 111–116.

[12] T.W. Kenny, W.J. Kaiser, S.B. Waltman, J.K. Reynolds, Novel infrared detector based on a tunneling displacement transducer, Appl. Phys. Lett. 59 (1991) 1820–1822.

[13] T.W. Kenny, J.K. Reynolds, J.A. Podosek, E.C. Vote, L.M. Miller, H.K. Rockstad, W.J. Kaiser, Micromachined infrared sensors using tunneling displacement transducers, Rev. Sci. Instrum. 67 (1996) 112–128.

[14] N.C. MacDonald, Single crystal silicon nanomechanisms for scanned-probe device arrays, Technical Digest, IEEE Solid-State Sensor Actuator Workshop, IEEE, New York, 1992, pp. 1–5.

[15] J.J. Yao, S.C. Arney, S.C. MacDonald, N.C. MacDonald, Fabrication of high frequency two-dimensional nanoactuators for scanned probe devices, J. Microelectromech. Syst. 1 (1992) 14–22.

[16] J.C. Jiang, V. Faynberg, R.C. White, P.K. Allen, Fabrication of micromachined silicon tip transducer for tactile sensing, J. Vac. Sci. Technol., B 11 (1993) 1962–1967.

[17] D. Kobayashi, T. Hirano, T. Furuhata, H. Fujita, An integrated lateral tunneling unit, Proceedings IEEE Micro Electro Mechanical Systems, An Investigation of Micro Structures, Sensors, Actuators, Machines and Robots IEEE, New York, 1992, pp. 214–219.

[18] A. Witek, D.G. Onn, Proposal for a novel magnetometer, J. Vac. Sci Technol., B 9 (1991) 639–642.

[19] R.C. Fenn, M.J. Gerver, R.L. Hockney, B.G. Johnson, J.L. Wallace, Microfabricated magnetometer using Young's modulus changes in magnetoelastic materials, Pro. SPIE — Int. Soc. Opt. Eng. 1694 (1992) 132–143.

[20] M. Chmielowski, A. Witek, Tunneling thermometer, Sens. Actuators, A 45 (1994) 145–151.

[21] C.W. Yeh, K. Najafi, Bulk-silicon tunneling-based pressure sensors, Technical Digest, Solid-State Sensors and Actuators Workshop, Transducer Research Foundation, Cleveland Heights, 1994, pp. 201–204.

[22] G. Binnig, C.F. Quate, Ch. Gerber, Atomic force microscope, Phys. Rev. Lett. 56 (1986) 930–933.

[23] G.U. Lee, D.A. Kidwell, R.J. Colton, Sensing discrete streptavidin–biotin interactions with atomic force microscopy, Langmuir 10 (1994) 354–357.

[24] G.U. Lee, L.A. Christy, R.J. Colton, Direct measurement of the forces between complementary strands of DNA, Science 266 (1994) 771–773.

[25] T.W. Kenny, W.J. Kaiser, H.K. Rockstad, J.K. Reynolds, J.A. Podosek, E.C. Vote, Wide-bandwidth electromechanical actuators for tunneling displacement transducers, J. MEMS 3 (1994) 97–104.

[26] L.H. Dubois, B.R. Zegarski, R.G. Nuzzo, Molecular ordering of organosulfur compounds on Au(111) and Au(100): adsorption from solution and in ultrahigh vacuum, J. Chem. Phys. 98 (1993) 678–688.

[27] W.T. Scott, The Physics of Electricity and Magnetism, Wiley, New York, 1966.

[28] H. Zijlstra, Rev. Sci. Instrum. 41 (1970) 1241.

[29] T.B. Gabrielson, Mechanical-thermal noise in micromachined acoustic and vibration sensors, IEEE Trans. Electron. Devices 40 (1993) 903–909.

[30] L. Stockman, H. Vloeberghs, I. Heyvaert, C. Van Haesendonck, Y. Bruynseraede, Topographic study of thin gold films grown on $SiO_2$, Ultramicroscopy 42–44 (1992) 1317–1320.

[31] R.C. Jaklevic, L. Elie, Scanning-tunneling-microscope observation of surface diffusion on an atomic scale: Au on Au(111), Phys. Rev. Lett. 60 (1988) 120–123.

[32] D.J. Trevor, C.E.D. Chidsey, Room temperature surface diffusion mechanisms observed by scanning tunneling microscopy, J. Vac. Sci. Technol., B 9 (1991) 964–968.

[33] S.J. Stranick, M.M. Kamna, K.R. Krom, A.N. Parikh, D.L. Allara, P.S. Weiss, Scanning tunneling microscopy studies of self-assembled monolayers of alkanethiols on gold, J. Vac. Sci. Technol., B 12 (1994) 2004–2007.

[34] S.A. Joyce, R.C. Thomas, J.E. Houston, T.A. Michalske, R.M. Crooks, Mechanical relaxation of organic monolayer films measured by force microscopy, Phys. Rev. Lett. 68 (1992) 2790–2793.

## Biographies

*Dan DiLella* received his PhD in Chemistry from the University of Massachusetts at Amherst in 1978. His research interests include sensors based on tunneling and sensors based on surface acoustic waves. He is associate professor of chemistry at Shepherd College and a part-time employee in the Functional Materials and Devices Section (Code 6375) at the Naval Research Laboratory.

*Lloyd J. Whitman* received his PhD in Physics from Cornell University in 1988. After a National Research Council Postdoctoral Fellowship at National Institute of Standards and Technology, he joined the Naval Research Laboratory in 1991 as a Research Physicist in the Chemistry Division. His research interests include the structure of surfaces as determined using scanning probe microscopy and the development of related sensor technologies. He is currently the head of the Surface Nanoscience and Sensor Technology Section (Code 6177).

*Richard J. Calton* is a supervisory research chemist and Head of the Surface Chemistry Branch at the Naval Research Laboratory (NRL). He earned his BS and PhD degrees from the University of Pittsburgh in 1972 and 1976, respectively. In 1976, he was a National Research Council Resident Research Associate at NRL working on secondary ion mass spectrometry. Dr. Colton joined the NRL staff in 1977 and conducts basic and applied research in surface chemistry. His current research interests include the measurement of the nanomechanical properties of materials using atomic force microscopy and the development of new sensors using electron tunneling and force transducers.

*Thomas W. Kenny* received the BS degree in Physics from the University of Minnesota, Minneapolis, MN, in 1983 and the MS and PhD degrees in Physics from the University of California, Berkeley, in 1987 and 1989, respectively. He has worked at the Jet Propulsion Laboratory (JPL), where his research focused on the development of electron-tunneling-based high-resolution microsensors. Since 1994, he has been Assistant Professor and Terman Fellow with the Mechanical Engineering Department, Stanford University, Stanford CA. He currently oversees graduate students in the Stanford Microstructures and Sensors Laboratory, whose research activities cover a variety of areas such as advanced tunneling sensors, novel fabrication techniques for micromechanical structures, and the use of MEMS devices and structures for force detection in many applications.

*William J. Kaiser* received his PhD from Wayne State University in 1983. His graduate work, completed while he was a member of the Ford Motor Research Staff, included the development of an automotive sensor system that later appeared in commercial vehicles. He went on to the JPL where he invented ballistic electron emission microscopy (BEEM) and worked on the development of the first electron tunnel sensor for MEMS. He is currently the chairman of the Electrical Engineering Department at the University of California, Los Angeles, where his research focuses on combining microsensors, low power electronics, and wireless network technology into compact, integrated packages for distributed monitoring and control. Applications have been demonstrated in the areas of manufacturing, medical and military information systems.

*Erika C. Vote* received the BS in Electrical Engineering at the Colorado School of Mines in 1992. Between college years, Ms. Vote spent summers working at the JPL as an engineering intern. In 1992, she joined the technical staff in Thomas Kenny's research group, where she was involved in the fabrication of tunneling infrared sensors, and in the design, fabrication, and testing of the tunneling magnetometer described in this report. She is co-author of the one patent and five technical publications, and received a 1993 R&D 100 Award for her work on the uncooled tunneling infrared sensor. Ms. Vote passed away in 1994.

*Judith A. Podosek* is a processing engineer at the MicroDevices Laboratory, JPL. In 1983, she began her technical career at The Aerospace Corporation where she was responsible for the growth, fabrication and characterization of GaAs/AlGaAs lasers. In 1987 she joined the photonics group at the JPL as a processing engineer where she continued to work with semiconductor laser materials focussing on metal organic chemical vapor Deposition (MOCVD) of GaAs/AlGaAs structures. In 1990, she joined JPL's MEMS effort in the area of electron tunneling devices. Her current research and development interests include magnetic-field sensors, navigation sensors, and sensor integration within JPL's System On A Chip (SOAC) program.

*Linda M. Miller* received her PhD in Electrical and Computer Engineering from the University of Illinois, Urbana-Champaign in 1991. Since then she has worked in the MEMS Technology Group at the JPL where she has led efforts in the areas of high-resolution MEMS sensors for space applications. She is currently the task manager for sensor integration in the System On A Chip (SOAC) program at JPL. Her research interests include nanotechnology and miniature laboratory systems. She is member of IEEE, AAAS, and is a program committee member of the "Science of MEMS" technical group for the American Vacuum Society.